

# AERODYNAMIC ANALYSIS OF TRANSITIONAL WINGS ENCOUNTERING HIGH AMPLITUDE STREAMWISE GUST

V. Ferrand<sup>(1)</sup> and E. R. Gowree<sup>(2)</sup>

<sup>(1)</sup> ISAE-SUPAERO, Toulouse university (France) [valerie.ferrand@isae-supaero.fr](mailto:valerie.ferrand@isae-supaero.fr)

<sup>(2)</sup> ISAE-SUPAERO, Toulouse university (France) [erwin-ricky.gowree@isae-supaero.fr](mailto:erwin-ricky.gowree@isae-supaero.fr)

## ABSTRACT

We are interested here in the effect of high amplitude streamwise gusts felt by fixed rigid wings at pre-stall angles of incidence in low Reynolds numbers ( $Re \approx 50 \times 10^3 - 200 \times 10^3$ ) flow conditions. An experimental rig has been developed to reproduce a cyclic variation of the freestream axial velocity representative of the perturbations micro-aerial vehicles can encounter in a urban environment. The temporal evolution of the aerodynamic forces (lift, drag and pitching moment) recorded during the gust show significant deviations from the quasi-static predictions that unsteady but inviscid methods are unable to capture. These deviations appear to be related to the dynamic of both the laminar separation bubble and the laminar separation without trailing edge reattachment, also known as the “short” and “long bubble” respectively.

## 1. INTRODUCTION

Unmanned aerial systems (UAS) or micro-aerial systems (MAS) are gradually paving their way into the urban environment for a diverse range of applications. However, the urban environment is seldom highly perturbed by a multitude of flow scales in the form of fine or large turbulent eddies or gusts emanating from the urban canyons, building wakes or the topology of the landscape. The forward speeds of the UASs and MASs and size of the latter is relatively low, of the order of a meter with operating speeds,  $U_\infty = 10 - 15m/s$  which are of the same order of the gusts or eddies in the perturbed environment [14], [9], [2]. These perturbations have been forecast to worsen due to climate change pose serious challenges for flight stability of the UAS or MAS. In order to ensure their reliable and safe operations specially in densely populated area it

is important to understand how they respond to such perturbation, so as to design systems which are more robust but without too much compromise to their endurance. Further understanding of the behaviour in such environment will allow us to improve of numerical prediction strategy for design and optimisation and also to development passive and/or active control strategies such as wing morphing.

Here, we are interested in the strong variations of the freestream wind along the line of fight, qualified as “longitudinal gust” felt by vehicles evolving at low Reynolds numbers,  $Re \approx 50 \times 10^3 - 200 \times 10^3$ . This kind of perturbation is rather scarce in the literature as opposed to the vertical gusts which act directly on the angle of attack and thus generate strong unsteady effects as soon as stall is approached dynamically. In this case the unsteadiness does not come from a change in effective incidence but is driven by oscillatory behaviour of the streamwise flow, thus an oscillatory boundary layer resulting in an unsteady drag force since it is strongly influenced by a time varying location of transition. In fact, at these Reynolds speeds, a laminar bubble develops on the suction surface of the wing and its time evolution (size / position) plays a decisive role in the unsteadiness of both the lift and drag forces due to a large distortion of the static pressure field [10], [9], [13], [4]. Thus, the inviscid theoretical models, classically used to predict unsteady lift for longitudinal gust [6] becomes questionable, even for flight angles of attack clear of stall, [13].

In the current experimental study, we propose to qualify the aerodynamic response of a quasi-infinite and finite span wing to sinusoidally oscillating freestream velocity input in the pre-stall regimes. In addition to the unsteady lift we will also characterise the unsteady drag which has received limited treatment in the literature. The behaviour of the unsteady aerodynamic forces has been fur-

ther analysed with coupled boundary layer measurements which provided a more conclusive understanding of the departure from the inviscid theory of Greenberg [6].

## 2. EXPERIMENTAL SET-UP AND GUST CHARACTERISTICS

An experimental rig has been developed at ISAE-SUPAERO to reproduce an oscillating longitudinal gust,  $U(t)$ , in an open circuit wind tunnel which has a square test section of sides  $0.45m$  and is  $3m$  long. The longitudinal flow oscillations is generated by oscillating louvre-doors located in the aft region of the working section as shown in Fig. 1. This imposes an additional but time-varying total-pressure loss downstream which in turn results in a reduction or increase in the flow speed, a technique recently implemented in other wind tunnels [7], [12], [4]. Here, an array of four plates controlled by independent by servomotors can achieve a maximum blockage 85% in the fully closed position (Fig. 1). The tests are conducted at reduced oscillation frequency,  $k = \frac{2\pi fc}{U_\infty} = 0.13$  where  $U_\infty$  designates the mean freestream flow velocity and  $c$  the wing chord. The oscillating freestream generated during the current experiment is shown in Fig. 2 and represents a gust ratio,  $\frac{\Delta(U)}{2*U_\infty} = 0.37$ , classifying it as "high amplitude" and weakly unsteady longitudinal gust according to ([1]). The chord based Reynolds number oscillated in the transitional regime with  $Re_{min} = 60000$  and  $Re_{max} = 140000$ .

The overall forces and moment were measured using a Deltalab 10N forced balance, with an estimated accuracy of 0.15% in the lift coefficient,  $C_L$ , and 0.26% on the drag coefficient  $C_D$  for the range covered during the experiment. Even if the balance on its own could attain much higher frequency response, the addition of the wing, supports and fixation, reduced the overall, cut-off frequency,  $f_c \approx 30Hz$  which was measured during a wind-off test. For further diagnostic of the unsteady nature of the flow constant temperature anemometry was employed. Here, two Dantec Dynamics (55R01) hot-film probes were used :a fixed one located (4 chords) upstream of the model to monitor the oscillating freestream flow and a second which could be positioned closer to the wing surface and displaced in the chordwise direction using a 2-axis traverse system to characterise the boundary layer. The probes were connected to Dantec Dynamics mini CTA where the cut-off frequency was at  $1kHz$ . The measurements in the boundary were conducted at a fixed wall-normal position ( $y = 0.6mm$ ) measured using the technique in [5] at all chordwise positions considered here. The freestream turbulence intensity was approximately 0.3% within a frequency band of 10 to 3kHz where the low frequency corresponds to the perturbation based on the length of the working section for the given

mean freestream velocity and the high frequency cut-off was fixed by the mini CTA.

The actuation of the servomotors, control and monitoring of the wind tunnel condition, synchronised force balance and hot film data acquisition were performed under Labview. The hot-film signal was sampled at  $f = 2kHz$ , which was deemed sufficient to capture the primary instability development in laminar separation bubbles from previous experience. Since all the measurements were synchronised or in phase with the upstream hot film, the force measurements were phase-averaged over 100 cycles. The experiment was conducted on three different wings with varying aspect ratio,  $AR$  but similar NACA0012 profile, here we will be presenting the results for  $AR = 6$ , which extended towards the extremities of the wall to approach an infinite span or 2D condition and a finite wing,  $AR = 3$ .



Figure 1: The experimental set-up showing the wing model at incidence and the array of louvre-door downstream.

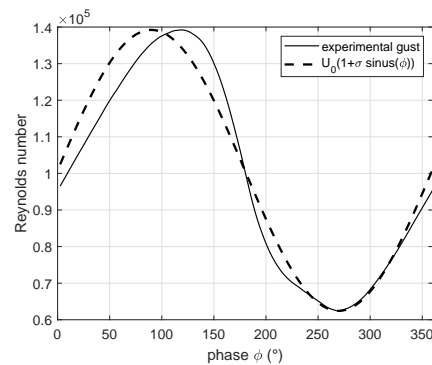


Figure 2: Unsteady freestream Reynolds number  $Re$  during the periodic surge cycle. dot line : sinusoidal evolution of equivalent amplitude  $\sigma$ .

### 3. QUASI-2D WING IN STEADY FREESTREAM

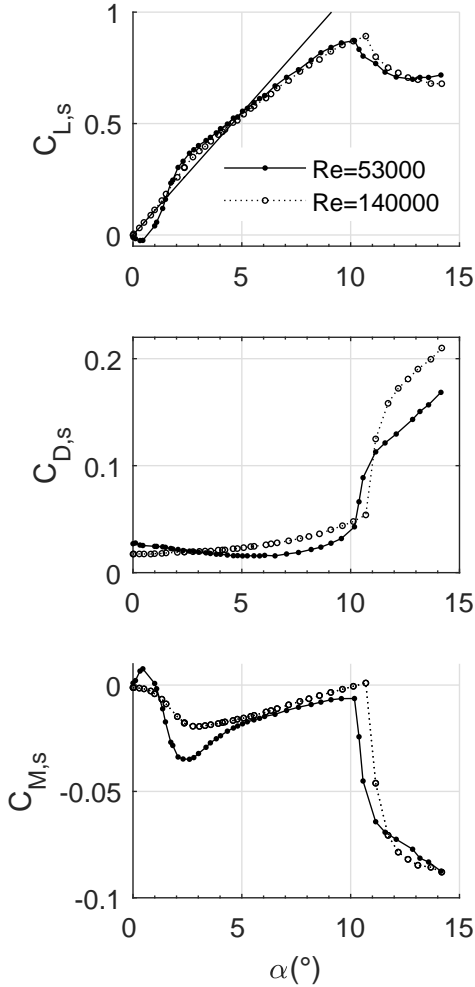


Figure 3: Lift, drag and pitching moment coefficients with angle of attack. The thin airfoil theory prediction  $C_L = 2\pi\alpha$  is reported on the top plot.

#### 3.1 The steady aerodynamic forces

Fig. 3 shows the evolution of the static lift coefficient,  $C_{L,s}(\alpha)$ , drag coefficient  $C_{D,s}(\alpha)$  and the pitching moment  $C_{M,s}(\alpha)$  about the quarter chord position, for the static freestream Reynolds number  $Re = 53 \times 10^3$  and  $Re = 140 \times 10^3$ , which correspond to the minima and maxima of the streamwise gust shown in Fig. 2. The time average data shown is for a sample of 20k at a sampling frequency of 500Hz. The large deviation in the pre-stall  $C_{L,s}$  with respect to the thin aerofoil inviscid theory is due

to the highly viscous characteristic of the flow as a consequence of the Reynolds number being fairly low. In this regime the flow is expected to be laminar, therefore susceptible to separation on the upper surface either in the form of laminar separation bubble (LSB) which reattaches to a turbulent boundary layer downstream referred as a “short bubble” or laminar separation without reattachment, known as “long bubble” according to Gaster [3]. The flow regime, long bubble or short bubble, is highly sensitive to Reynolds number and angle of attack. The extended separated region has a stronger effect on the pressure distribution, this produces the non-linear behaviour in the overall aerodynamic forces and moment [15], [8]. The resulting pressure plateau region already has noticeable effect on the pre-stall  $C_{L,s}$  and  $C_{M,s}$  as seen in Fig 3, whereas on the  $C_{D,s}$  the effect can be split as competition between form drag and skin friction drag which is significantly influenced by separation and transition to turbulence respectively.

For the case of  $Re = 53 \times 10^3$  the unusual negative slope in  $C_{L,s}$  for  $0^\circ < \alpha \leq 1^\circ$  was a consequence of the laminar separation (long bubble) which extended towards the trailing edge of the suction surface (the surface with peak suction at leading edge) and this observation can be supported by the positive  $C_{M,s}$ , a upward pitching moment due to non-negligible rear unloading. After reaching a minima further increase in incidence led to the more usual trend in  $C_L$  however at a rate higher than the thin aerofoil theory,  $dC_L/d\alpha = 2\pi$ , as seen in the top of Fig. 3 for  $1^\circ < \alpha \leq 3^\circ$ . This range of incidence encountered negative pitching moment which was due to the competition between the contribution from the laminar separation bubble and the drop in the suction peak, when compared to an inviscid case where the pitching moment is expected to be zero. From the top left of Fig. 4 a remarkable agreement was observed with XFRL5 in this  $\alpha$  regime, for an N-factor of 8 confirming that this behaviour was not an artifact due to inaccuracy of the force balance in measuring the small forces. This was accompanied by a drop in  $dC_L/d\alpha$  for  $\alpha > 3^\circ$ , here the slope from the experimental results agreed quite well with that from XFRL5, however this comparison was improved marginally with reduction in N-factor as opposed to the case of lower incidence.

To further characterise these two pre-stall regimes a simple but well established approach for the identification of buffet onset is applied here. At high Reynolds number the buffet onset can be identified by tracking the departure of  $dC_L/d\alpha$  from a constant value, not strictly  $2\pi$  as in the case of finite wings. This departure is due to strong viscous flow effect not modelled by thin aerofoil theory, as in the case of separation which introduces non-linearity, thus indicating the shift to a different flow regime. From the bottom left of Fig. 4, as mentioned earlier the negative slope is encountered for alpha  $0^\circ < \alpha \leq 1^\circ$ , this slope increases rapidly for higher  $\alpha$

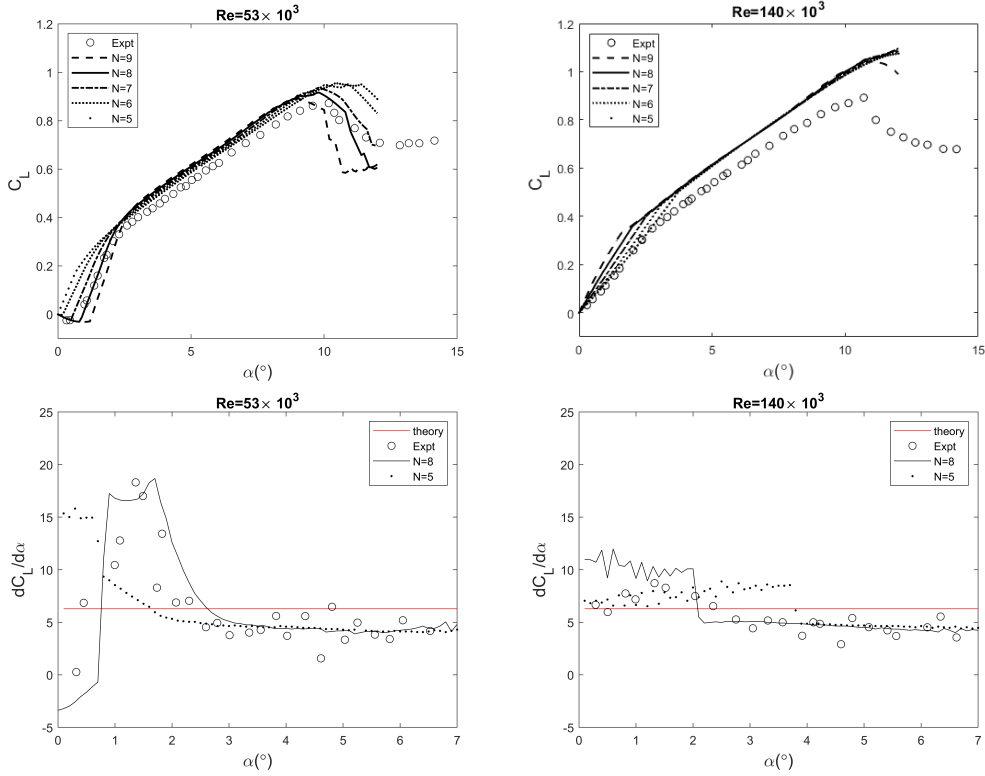


Figure 4: Comparison of the experimentally measured  $C_{L,s}$  with those calculated by XFLR5 at different N-Factor (top) and the rate of change in  $dC_L/d\alpha$  (bottom) for  $Re = 53 \times 10^3$  and  $Re = 140 \times 10^3$  on the left and right respectively.

even surpassing the value from thin aerofoil theory with a peak at  $\alpha \approx 2^\circ$ . It decreases thereafter and starts to plateau at  $\alpha \approx 3^\circ$  and remains constant in the pre-stall region at a value below the  $2\pi$ . This indicates a fully established regime and the pressure and wall shear stress distribution from XFLR5 showed that it was due to the presence of a laminar separation bubble (short bubble) which propagates upstream and reduces in length with increasing incidence. Whereas, for the case of  $0^\circ < \alpha < 2^\circ$  XFLR5 showed another regime which consisted of a laminar separation without turbulent reattachment (long bubble). The higher values of  $dC_L/d\alpha$  was potentially due to enhanced suction from the large region of the separated flow, as in the case of leading edge vortices.

At  $Re = 140 \times 10^3$ , the negative slope in  $dC_L/d\alpha$  was not present as seen from the XFLR5 calculations on the top left of Fig. 4, however at low angle of incidence the agreement between experiment and XFLR5 was improved with lower N-factor, which collapsed together at higher pre-stall angle of incidence. Once again, despite some differences in the absolute magnitude the overall slope between the experiment and XFLR5 results are quite consistent. The wall shear stress distribution from XFLR5 showed that here the flow was dominated by the presence of laminar separation bubble which reattaches as a turbulent boundary layer downstream, therefore a

short bubble. Unlike in the case of the of  $Re = 53 \times 10^3$ , here the contribution of the pressure plateau to the overall lift is expected to be lower, which explains the lower variation in  $dC_L/d\alpha$  on the bottom left of Fig. 4.

Although, XFLR5 does not permit boundary layer stability analysis and the N-factor approach has not been thoroughly validated on laminar separation problem, when comparing the prediction from XFLR5, on top of Fig. 4 the agreement between the experiment and XFLR5 is not intuitive with the N-factor. In the case of  $Re = 53 \times 10^3$ , for  $0^\circ < \alpha \leq 2.5^\circ$ , where the long bubble was expected a better agreement was observed at high N-factor, whereas for  $\geq 2.5^\circ$ , expected to have a short bubble, the agreement was improved at lower N-factor similarly for the case of  $Re = 140 \times 10^3$  where a short bubble was expected for all pre-stall angle of incidence. Considering the fairly high turbulence intensity level of the wind tunnel (approximately 0.3%), the  $N \approx 4$  from Crouch's criterion. Unreported measurements at ISAE-SUPAERO and Onera Toulouse have shown that at this  $Tu$  an LSB is still active but is much smaller compared to lower  $Tu$  cases since the amplification rate is higher but still follows modal linear stability.

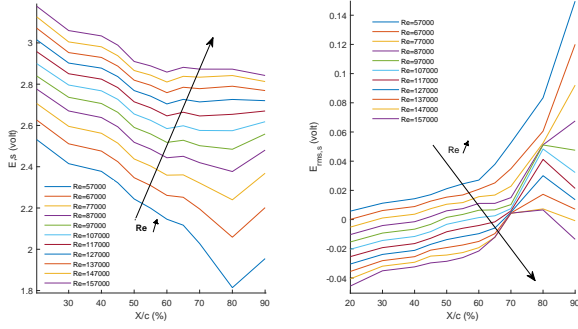


Figure 5: Mean hot film signal  $E_s$  (on the left) and fluctuations  $E_{rms,s}$  (on the right) in the boundary layer at a fixed distance from the surface, for various upstream Reynolds numbers. For more clarity,  $E_{rms,s}$  have been shifted by a negative value increasing with the Reynolds number.

### 3.2 Characterisation of the boundary layer

In order to further confirm the presence of the two regimes observed from the overall force and moment measurements, the state of the boundary layer was further characterised for an incidence of  $\alpha = 2.5^\circ$  using a hot film positioned at a fixed wall normal position of  $y \approx 0.6mm$  for chordwise locations ranging between  $20\% \leq x/c \leq 90\%$ . The voltage signal  $E(t)$  from the hot film is proportional to the velocity in the boundary layer therefore a low momentum fluid will result in low hot film signal. In Fig. 5 we observe that the average value of the hot film voltage  $E_s$  recorded at a fixed position  $x/c$  increases with increasing freestream Reynolds number. This is due to the increase in the external velocity itself and the resulting reduction of the boundary layer thickness will lead to an increase in momentum or heat transfer and hence higher voltage or velocity for a fixed wall normal position as opposed thicker boundary layer. While moving downstream, due to the adverse pressure gradient, the external velocity reduces and similarly for a fixed wall normal position the hot wire voltage will reduce due to reduction in heat transfer. Since the hot-film is direction insensitive the reverse flow in the separated zones cannot be resolved, however in this low momentum zone there is very low heat transfer resulting in significant drop in voltage seen around  $x/c \approx 70\%$  in Fig. 5 for the low Reynolds number cases. However, the voltage starts to increase again for  $x/c \geq 80\%$ , this introduces some doubt on whether the boundary layer had reattached into a turbulent state. But from the figure on the left, the  $E_{rms,s}$  continues to increase suggesting the presence of a “long bubble”.

For higher Reynolds number cases,  $Re \geq 100 \times 10^3$ , the chordwise location at which the rise in voltage occurs is shifted upstream, this indicates a reduction in the length of the laminar separation bubble.

Without the actual velocity profile, the above explanation possesses some weaknesses especially due to the presence of the pressure gradient. In this case the state of the boundary layer could be better characterised by the levels of fluctuations. These have been plotted in terms of  $E_{rms,s}$  on the right of Fig. 5. For all Reynolds number, at  $x/c \approx 70\%$  a sharp rise in  $E_{rms,s}$  is observed and this would confirm the rapid amplification of instability mode which would be expected in an LSB. The upstream shift in the position of rapid rise in  $E_{rms,s}$  with increasing Reynolds number would therefore indicate a shift in the position of the LSB which also appears to shrink due to the slight reduction of the  $E_{rms,s}$  which is expected from the turbulent reattachment.

The above analysis could be further complemented with the spectra at various chordwise positions for three Reynolds numbers shown in Fig. 6. For  $Re = 157 \times 10^3$  there is clear evolution of the high energy content which starts to fill in a larger band of frequencies when moving towards the trailing edge and this will indicate the shift in the spectra from a laminar boundary layer to a turbulent where the energy is spread over a larger band of frequency. In this case, it will be fair to assume that at  $x/c \geq 60\%$  the separation bubble reattaches to a turbulent boundary layer. This effect is slightly retarded to  $x/c \geq 70\%$  for the intermediate Reynolds number,  $Re = 107 \times 10^3$ , which indicates the enlargement of the separation bubble. In addition, at  $x/c \approx 70\%$ , the narrow frequency band centred at around  $f = 370Hz$  potentially corresponds to the dynamics of the separation bubble. But for the lowest Reynolds number case,  $Re = 57 \times 10^3$ , for none of the chordwise position the spectra showed the earlier mentioned turbulent characteristics even at the most downstream measurement position,  $x/c = 90\%$ . At this position and at  $x/c = 80\%$  a growth in energy was observed over a larger frequency band of  $105Hz \leq f \leq 265Hz$  which potentially corresponds to a larger region of separated flow without reattachment, but this would require further confirmation since the hot-film measurements were limited to  $x/c = 90\%$ .

## 4. QUASI-2D WING SUBJECTED TO STREAMWISE GUST

### 4.1 Characterisation of the oscillating boundary layer

Here we will start by characterising the state of the oscillating boundary layer, when the wing is subjected to a longitudinal gust. On the left of Fig. 7 the raw time-varying voltage,  $E(t)$  from the hot film during periodic streamwise gusts for different positions along the profile are shown for a fixed angle of incidence  $\alpha = 2.5^\circ$ . On the right of Fig. 7, the same signal is filtered by a high pass filter (cutoff frequency  $10Hz$ ) and denoted as  $E_{HF}$ . As of

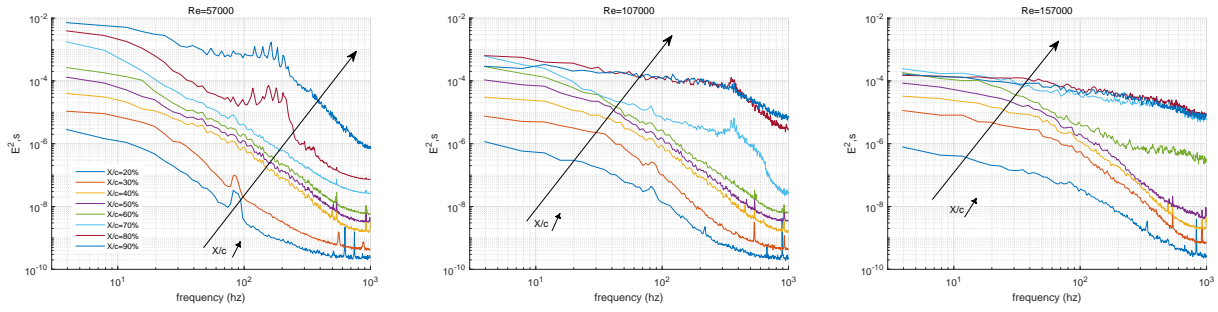


Figure 6: Spectra of the hot wire signal for 3 freestream Reynolds number  $Re = 57000$ ,  $Re = 107000$  and  $Re = 157000$  at various  $X/c$  locations along the airfoil. Spectrum are shifted by positive values increasing with  $X/c$ .

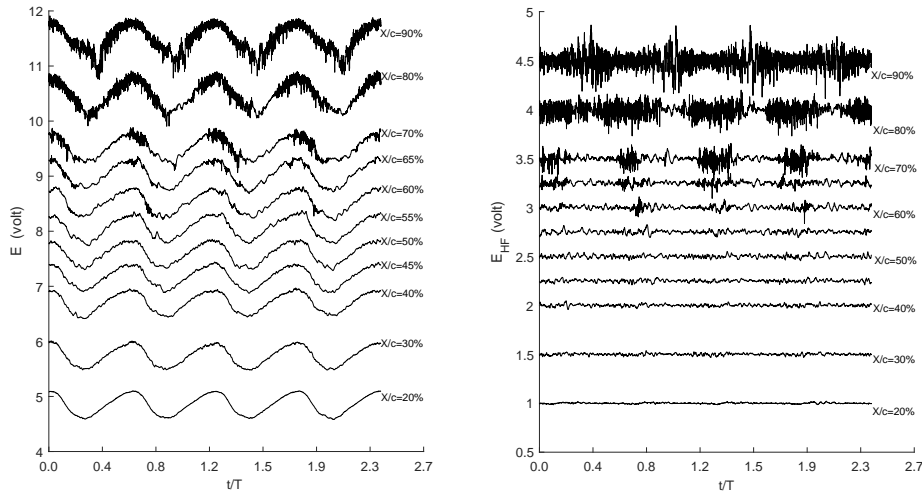


Figure 7: Time-series of the raw hot-film voltage  $E(t)$  (left) and the corresponding high pass filtered  $E_{HP}(t)$  (right) during 4 successive streamwise gusts at various  $x/c$  locations along the airfoil. Signals have been shifted by a positive value increasing with  $x/c$ .

$X/c > 40\%$  some jaggedness in the low frequency oscillating hot film signal is already apparent in Fig. 7 and at  $X/c > 50\%$  turbulent spots can be seen in the deceleration zones of the cycle. At first the large fluctuations from the turbulent spots are straight after the peak in the cycle but starts spreading over a larger portion of the cycle when moving towards the trailing edge. This can be confirmed from the filtered signal on the right of Fig. 7. At  $X/c = 90\%$ , the entire cycle has become turbulent. The transition of the boundary layer on the deceleration phases of the cycle highlights an asymmetry in the behavior of the flow between the two parts of the cycle: at equivalent speed, the flow is laminar in the acceleration phases and turbulent in the deceleration phases.

The left and right of Fig. 8 represent the phase averaged of the hot film signal  $E(\phi)$  and the associated average fluctuation  $E_{HFrms}(\phi)$  respectively, obtained by over 15 consecutive cycles. The average signal  $E, qs(\phi)$  associated with a quasi-static gust is also plotted for compar-

ison. Up to  $x/c \leq 40\%$ , almost negligible difference between the unsteady and quasi-static mean, voltage, velocity or heat flux is detected. This suggest that the attached laminar boundary layer upstream responds to the streamwise oscillations in a quasi-static way. At  $X/c > 70\%$ , a pronounced phase shift appears between the two signals  $E(\phi)$  and  $E, qs$  around  $(\phi \approx 270^\circ)$ . This behavior is associated with boundary layer separation. This phenomenon, which appears over part of the cycle and elongated close to the trailing edge of the profile, is characterized by a very weak signal  $E(\phi)$  and very strong fluctuations  $E_{HFrms}(\phi)$  as shown in on the right of Fig. 9 and seems to be a local enlarged separation area referred as “SS” in Fig. 9.

To highlight the dynamics of the LSB and the potential trailing edge separation from a long bubble due to the streamwise oscillations, a spatio-temporal representation of the mean heat flux  $E(x/c, \phi)$ , which is directly proportional to the velocity and its fluctuations  $E_{HFrms}(x/c, \phi)$

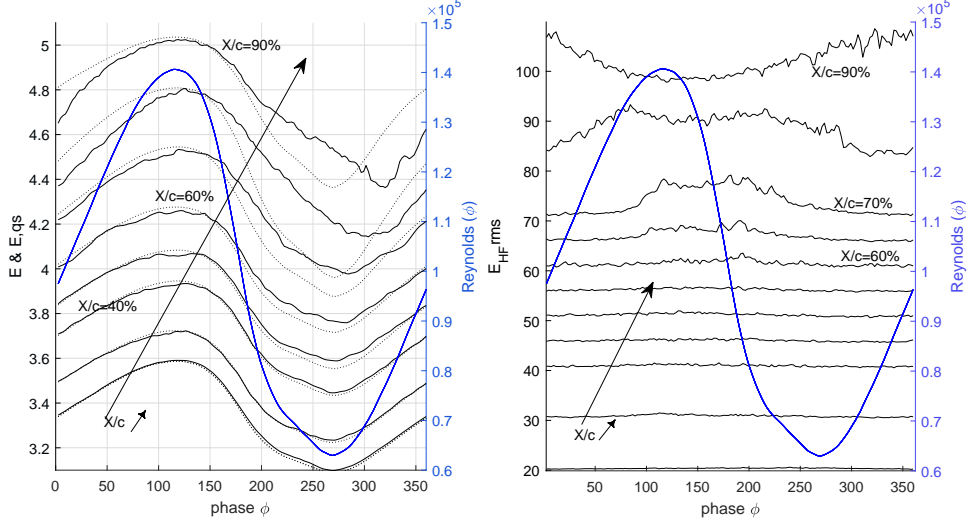


Figure 8: Phase average hot-film voltage  $E$  (top plot) and the corresponding rms values  $E_{rms}$  (bottom plot) at various  $X/c$  locations along the airfoil. Signals have been shifted by a positive value increasing with  $X/c$ . dot lines : hot-film mean voltage  $E_{qs}$  in quasi-static approach.

are presented in Fig. 9. At  $\alpha = 2.5^\circ$ , the exact position and the length of LSB is cannot be easily detected from the current hot-film measurements. Nevertheless, for each phase  $\phi^*$  of the cycle, the origin of the laminar separation can be estimated when  $E_{HF rms}(X/c, \phi^*)$  begins to increase rapidly. This regions is estimated for a few key phases in Fig. 9 and denoted by  $S_L$ . The transition point  $T$  is estimated at the point where the fluctuations reach their maximum and the reattachment, if it takes place, when the fluctuations decrease again. At each instant of the cycle, the separation bubble can therefore be identified between the region bounded by  $S_L$  and  $A_T$  in Fig. 9 (bottom). Thus, it appears that the LSB lengthens during the deceleration profile of the gust to reach its maximum length at  $\phi = 180^\circ$ , the phase associated with the maximum rate of deceleration. We also observe that close to the trailing edge at the very end of deceleration and over a large part of the acceleration ( $260^\circ \leq \phi \leq 360 + 70^\circ$ ), the flow potentially does not reattach but on the contrary gives way to an enlarged separation  $SS$ .

## 4.2 The unsteady aerodynamic forces

The unsteady forces due to the longitudinal gust are analysed by phase averaging over 100 cycles acquired at a frequency of 500Hz and high-pass filtered at 5Hz. The aerodynamic coefficients  $C_L(\phi)$  and drag  $C_D(\phi)$  are normalized by the instantaneous speed as shown below.

$$C_L(\phi) = \frac{L(\phi)}{1/2\rho U^2(\phi)c}; C_D(\phi) = \frac{D(\phi)}{1/2\rho U^2(\phi)c} \quad (1)$$

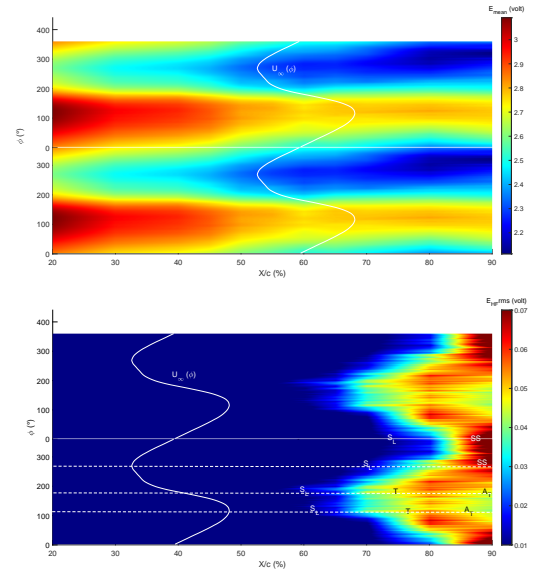


Figure 9: Phase-space variations of the phase average hot-film voltage  $E$  (top graph) and the corresponding rms values  $E_{rms}$  (bottom graph).

Under the effect of the streamwise gust, from Fig. 10 the phase averaged unsteady aerodynamic forces  $C_L(\phi)$  and  $C_D(\phi)$  show strong deviations from their quasi-static counterparts  $C_{L,qs}(\phi)$  and  $C_{D,qs}(\phi)$ , for all the angles of incidence  $\alpha$ . From Fig. 2, the initial acceleration occurs at  $0 < \phi < 120^\circ$ . The phase averaged  $C_L(\phi)$  is there lower than the quasi-static case, which is clearer on the bottom left of Fig. 10 as  $C_L(\phi)/C_{L,qs}(\phi)$  lies below a value of 1. On the other hand, in the deceleration phase,  $120^\circ <$

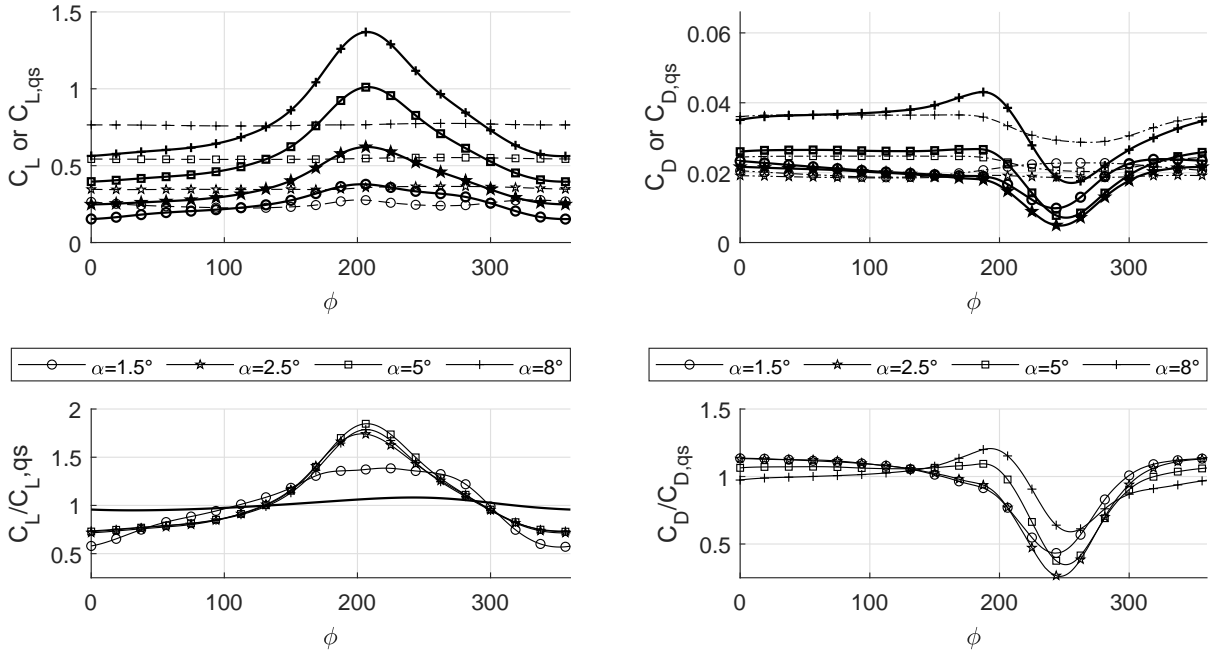


Figure 10: Phase average lift coefficient  $C_L$  for different angles of attack. dot lines : corresponding quasi-static predictions  $C_{L,qs}$ . black line : potential flow prediction (Greenberg theory [6]).

$\phi < 270^\circ$ , the value of 1 is exceeded indicating that the unsteady lift is higher than the static counterpart.

The  $C_L(\phi)$  is equivalent to 74% of  $C_{L,qs}$  at the instant of maximum acceleration ( $\phi = 0^\circ$ ) and 180% of  $C_{L,qs}$  at  $\phi = 207^\circ$  shortly after the maximum deceleration. The evolution of  $C_L(\phi)/C_{L,qs}(\phi)$  being remarkably insensitive to the angle of incidence, for all incidences  $1.5^\circ < \alpha \leq 8^\circ$ . On the right of Fig. 10 the unsteady drag coefficient shows a behavior more dependent on the angle of incidence  $\alpha$ . The sharp drop in drag observed at  $\phi = 245^\circ$  (minimum freestream velocity) for  $\alpha = 2.5^\circ$ , where  $C_D \approx 26\%$  of  $C_{D,qs}$ , is twice less than the case of  $\alpha = 8^\circ$  and slightly out of phase. Moreover, a drag increment is observed at  $\phi \approx 190^\circ$  for  $\alpha = 5^\circ$  (up to 110% of  $C_{D,qs}$ ) and  $\alpha = 8^\circ$  (up to 120% of  $C_{D,qs}$ ) as opposed to the case of  $\alpha = 1.5^\circ$  and  $\alpha = 2.5^\circ$  which are at similar levels.

In section 4.1 the dynamics of the boundary layer subjected to the longitudinally oscillating freestream was discussed for  $\alpha = 2.5^\circ$  and in this Reynolds number regime, the viscous effect is so dominant that it was seen to have significant influence on both the lift and the drag. Indeed, the elongation of the LSB in the deceleration phase would induce an additional depression on the upper surface, as seen earlier so this could explain additional lift in the peak observed at  $\phi = 207^\circ$ . The unsteady behavior of drag is more complex because it results from the contribution of friction drag and pressure or form drag. The

trailing edge separations appearing at the end of deceleration can explain the drop in frictional drag observed in this part of the cycle. When the angle of attack increases, the contribution of the pressure drag also increases and the strengthening of the laminar bubble in the deceleration zone generates not only lift but also pressure drag.

## 5. FINITE SPAN WING SUBJECTED TO STREAMWISE GUST

The unsteady force measurements on the finite wing with aspect ratio,  $AR = 3$ , are presented here. The aim was to identify to what extent the presence and dynamics of the tip vortex can modify the response of the finite span wing to a longitudinally oscillating streamwise flow compared to the 2D reference case. We observe an unsteady behavior of the lift coefficient quite similar to the 2D case with an increase rate of 180% around  $\phi = 200^\circ$  for  $\alpha \geq 5^\circ$  compared to the quasi-static predictions in Fig. 11, however the case of  $\alpha = 2.5^\circ$  showed a lower growth rate of approximately 150%.

With regard to the unsteady response of the drag coefficient, we find a more drastic increase around  $\phi = 200^\circ$  which is higher compared to the 2D case, and increases with increasing incidence where for  $\alpha = 8^\circ$ , the instantaneous drag  $C_D$  is almost 150% higher than the quasi-static prediction  $C_{D,qs}$  at this phase location as shown in Fig. 11. This behavior is attributed to the increase in in-

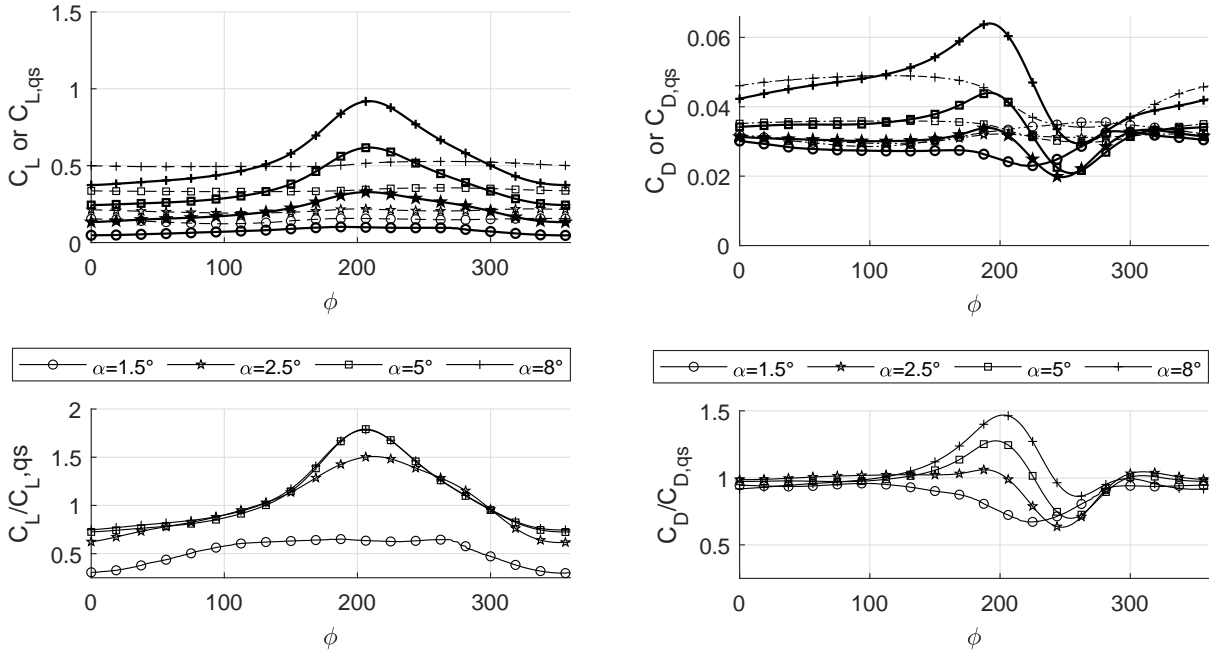


Figure 11: Phase average lift  $C_L$  and drag coefficients  $C_D$  for different angles of attack for the  $AR = 3$  wing. Dotted lines corresponds to the quasi-static case  $C_{L,q,s}$ .

duced drag which intensifies when the angle of attack increases. On the other hand, the drop in drag around  $\phi = 200^\circ$ , attributed to the separation of the trailing edge, is lower compared to the 2D reference and decreases when the angle of attack was increased. This behavior can be explained by the presence of the tip vortex which interacts with the separated region promoting earlier transition and turbulent reattachment from the suction surface [11]. Additional measurements will be required to confirm these hypotheses. The aerodynamic forces recorded for the lowest angle of attack,  $\alpha = 1.5^\circ$  shows a contrasting behaviour especially the drag coefficient for  $120^\circ < \phi < 270^\circ$ , therefore further boundary layer diagnostics will be required as this angle of incidence and Reynolds number regime was seen to be susceptible to the formation of a long bubble instead of a short bubble or LSB.

## 6. SUMMARY AND FURTHER WORKS

An experimental rig has been developed to reproduce an oscillating longitudinal gust representative of the perturbation that MASs or UASs can encounter in a perturbed urban environment. The gust ratio is approximately 0.37 with a reduced frequency,  $k = 0.13$ . While the reduced frequency remains moderate, the temporal evolution of the forces recorded during the gust show significant deviations from the quasi-static predictions that unsteady but

inviscid methods are unable to capture. During the decelerating part of the gust, a lift overshoot exceeding the quasi-static prediction by 180% is observed. This overshoot is visible regardless of the wing span and the angle of attack studied. It seems to be related to the laminar bubble elongation during this part of the surge cycle. Our contribution to the existing literature relies on the evolution of the unsteady drag force. When coming through minimum speed, drag can be reduced to 26% compared to quasi-static predictions. This significant undershoot and associate phase lag appears to be a consequence of unsteady trailing edge separation which reduces friction drag. The presence of the tip vortex, the intensity of which is reinforced when the incidence increases, modulates the temporal evolution of the drag. A drag overshoot, attributed to pressure drag, appears in phase with the lift overshoot during the maximum deceleration of the freestream flow.

These physical interpretations are based on preliminary measurements of the oscillating boundary layer. It will be necessary to supplement these measurements with those over a wider range of incidence and by spatio-temporal measurements by capturing unsteady velocity field using time-resolved PIV. These new measurements should shed new light on the dynamics of the laminar separation bubble and the trailing edge separation, short and long bubble respectively.

## ACKNOWLEDGMENTS

The authors are grateful for the technical support provided by Mr M. Grellet, S. Belliot and the DAEP technical team. Also the contribution of C. Korbuly an M. Sujiyama.

## REFERENCES

- [1] C. Badrya, B. Govindarajan, and Chopra. Basic understanding of unsteady airfoil aerodynamics at low reynolds numbers. In *2018 AIAA Aerospace Sciences Meeting*, Kissimmee, Florida, 2018.
- [2] A. J. Berry, J. Howitt, D.W. Gu, and I. Postlethwaite. A continuous local motion planning framework for unmanned vehicles in complex environments. *Journal of Intelligent and Robotic Systems*, 66:477–494, 2012.
- [3] M. Gaster. The structure and behaviour of laminar separation bubbles. Technical report, ARC RM3595, 1969.
- [4] D. Gloutak, K.E. Jansen, and A. John Farnsworth. Impact of streamwise gusts on the aerodynamic performance of a finite-span wing. In *AIAA SCITECH 2022 Forum*.
- [5] E. R. Gowree, C. J. Atkin, and S. Gruppetta. A simple digital-optical system to improve accuracy of hot-wire measurements. *Measurement Science and Technology*, 26(9):095303, 2015.
- [6] J. M. Greenberg. *Airfoil in Sinusoidal Motion in a Pulsating Stream*. 1947.
- [7] D. Greenblatt. Unsteady low-speed wind tunnels. *AIAA journal*, 54(10):1817–1830, 2016.
- [8] R. F. Huang, W. W. Shy, S. W. Lin, and F. Hsiao. Influence of surface flow on aerodynamic loads of a cantilever wing. *AIAA Journal*, 34(3):527–532, 1996.
- [9] A. R. Jones, O. Cetiner, and M. J. Smith. Physics and modeling of large flow disturbances: Discrete gust encounters for modern air vehicles. *Annual Review of Fluid Mechanics*, 54(1):469–493, 2022.
- [10] D. Jones and O. Cetiner. Overview of unsteady aerodynamic response of rigid wings in gust encounters. *AIAA journal*, 59(2):716–721, 2021.
- [11] D. Kim and M. Gharib. Experimental study of three-dimensional vortex structures in translating and rotating plates. *Experiments in Fluids*, 49(3):329–339, 2010.
- [12] R. Rennie, B. Catron, M. Zubair Feroz, D. Williams, and X. He. Dynamic behavior and gust simulation in an unsteady flow wind tunnel. *AIAA Journal*, 57(4):1423–1433, 2019.
- [13] C. Strangfeld, H. Müller-Vahl, C. N. Nayeri, C. O. Paschereit, and D. Greenblatt. Airfoil in a high amplitude oscillating stream. *Journal of Fluid Mechanics*, 793:79–108, 2016.
- [14] S. Watkins, J. Milbank, B. J. Loxton, and W. H. Melbourne. Atmospheric winds and their implications for microair vehicles. *AIAA journal*, 44(11):2591–2600, 2006.
- [15] J. Winslow, H. Otsuka, Govindarajan B., and I. Chopra. Basic understanding of airfoil characteristics at low reynolds numbers. *Journal of Aircraft*, 55(3):1050–1061, 2018.